Acoustic Signatures in the Primary Microwave Background Bispectrum

Eiichiro Komatsu* and David N. Spergel†

Department of Astrophysical Sciences, Princeton University, Princeton, NJ 08544, USA.

If the primordial fluctuations are non-Gaussian, then this non-Gaussianity will be apparent in the cosmic microwave background (CMB) sky. With their sensitive all-sky observation, MAP and Planck satellites should be able to detect weak non-Gaussianity in the CMB sky. On large angular scale, there is a simple relationship between the CMB temperature and the primordial curvature perturbation: $\Delta T/T = -\Phi/3$. On smaller scales; however, the radiation transfer function becomes more complex. In this paper, we present the angular bispectrum of the primary CMB anisotropy that uses the full transfer function. We find that the bispectrum has a series of acoustic peaks that change a sign, and a period of acoustic oscillations is twice as long as that of the angular power spectrum. Using a single non-linear coupling parameter to characterize the amplitude of the bispectrum, we estimate the expected signal-to-noise ratio for COBE, MAP, and Planck experiments. In order to detect the primary CMB bispectrum by each experiment, we find that the coupling parameter should be larger than 600, 20, and 5 for COBE, MAP, and Planck experiments, respectively. Even for the ideal noise-free and infinitesimal thin-beam experiment, the parameter should be larger than 3. We have included effects from the cosmic variance, detector noise, and foreground sources in the signal-to-noise estimation. Since the simple inflationary scenarios predict that the parameter is an order of 0.01, the detection of the primary bispectrum by any kind of experiments should be problematic for those scenarios. We compare the sensitivity of the primary bispectrum to the primary skewness and conclude that when we can compute the predicted form of the bispectrum, it becomes a "matched filter" for detecting the non-Gaussianity in the data, and much more powerful tool than the skewness. For example, we need the coupling parameter of larger than 800, 80, 70, and 60 for each relevant experiment in order to detect the primary skewness. We also show that MAP and Planck can separate the primary bispectrum from various secondary bispectra on the basis of the shape difference. The primary CMB bispectrum is a test of the inflationary scenario, and also a probe of the non-linear physics in the very early universe.

I. INTRODUCTION

Why measure the bispectrum of the cosmic microwave background (CMB) radiation anisotropy? Simple inflationary models predict that the CMB anisotropy field is nearly random Gaussian, and that two-point statistics completely specify statistical properties of CMB. However, our universe may not be so simple. Higher order statistics, such as the three-point correlation function, or its harmonic transform, the angular bispectrum, are potential probes of the physics of generating the primordial fluctuations. Since gravitationally induced non-linearities are small at $z \sim 1300$, CMB is expected to be the best probe of the primordial non-Gaussianity [1].

In the inflationary scenario [2–5], the quantum fluctuations of the scalar (inflaton) field generate the observed matter and radiation fluctuations in the universe [6–9]. In the stochastic inflationary scenario of Starobinsky [10], the quantum fluctuations decohere to generate the classical fluctuations. There are two potential sources of non-Gaussianity in this inflationary model: (a) the non-linear coupling between the classical inflaton field and the observed fluctuation field, and (b) the non-linear coupling between the quantum noise field and the classical fluctuation field. The former has been investigated by Salopek and Bond [11], while the latter has been explored by Gangui et al. [12]. Calzetta and Hu [13] and Matacz [14] present an alternative treatment of the decoherence process that leads to different results for the primordial density perturbation from those obtained by Starobinsky [10]. Matacz's treatment makes similar predictions for the level of non-Gaussianity to the Starobinsky's treatment [14]. These studies conclude that in the slow roll regime, the fluctuations are Gaussian. However, features in the inflaton potential can produce significant non-Gaussianity [15].

---

[1] komatsu@astro.princeton.edu; also at the Astronomical Institute, Tohoku University, Aoba, Sendai 980-8578, Japan.
[2] dns@astro.princeton.edu

There have been claims for both the non-detection [16] and the detection [17,18] of the non-Gaussianity in the COBE map. Banday, Zaroubi and Górski [19] argued the non-cosmological origin of the COBE non-Gaussianity. MAP and Planck will measure the fluctuation field down to angular scales $\simeq 0°\!.2$ and $0°\!.1$, and test these claims.

Previous work on the primary non-Gaussianity has focused on very large angular scale, where the temperature fluctuations trace the primordial fluctuations. This is valid on the COBE scale. For MAP and Planck; however, we need the full effect of the radiation transfer function. In this paper, we develop a formalism for doing this, and then present numerical results. Both the formalism and the numerical results are main results of this paper. We also discuss how well we can separate the primary bispectrum from various secondary bispectra.

This paper is organized as follows. Sec. II defines the bispectrum, the Gaunt integral, and particularly the new quantity called the "reduced" bispectrum, which plays a fundamental role in estimating the physical property of the bispectrum. Sec. III formulates the primary bispectrum that uses the full radiation transfer function, and presents the numerical results of the primary bispectrum and the skewness. Sec. IV estimates the secondary bispectra from the coupling between the Sunyaev–Zel'dovich and the weak lensing effects [20–22], and from the extragalactic radio and infrared sources. Sec. V studies how well we can measure each bispectrum, and how well we can discriminate among various bispectra. Sec. VI is devoted to further discussion and our conclusion.

II. DEFINING THE "REDUCED" BISPECTRUM

The observed CMB temperature fluctuation field $\Delta T(\hat{\mathbf{n}})/T$ is expanded into the spherical harmonics:

$$a_{lm} \equiv \int d^2\hat{\mathbf{n}} \frac{\Delta T(\hat{\mathbf{n}})}{T} Y^*_{lm}(\hat{\mathbf{n}}), \tag{1}$$

where hats denote unit vectors. The CMB angular bispectrum is given by

$$B^{m_1 m_2 m_3}_{l_1 l_2 l_3} \equiv \langle a_{l_1 m_1} a_{l_2 m_2} a_{l_3 m_3} \rangle, \tag{2}$$

and the angle-averaged bispectrum is defined by

$$B_{l_1 l_2 l_3} \equiv \sum_{m_1 m_2 m_3} \begin{pmatrix} l_1 & l_2 & l_3 \\ m_1 & m_2 & m_3 \end{pmatrix} B^{m_1 m_2 m_3}_{l_1 l_2 l_3}, \tag{3}$$

where the matrix is the Wigner-3j symbol. The bispectrum $B^{m_1 m_2 m_3}_{l_1 l_2 l_3}$ must satisfy the triangle conditions and selection rules: $m_1 + m_2 + m_3 = 0$, $l_1 + l_2 + l_3 =$ even, and $|l_i - l_j| \leq l_k \leq l_i + l_j$ for all permutations of indices. Thus, $B^{m_1 m_2 m_3}_{l_1 l_2 l_3}$ consists of the Gaunt integral, $\mathcal{G}^{m_1 m_2 m_3}_{l_1 l_2 l_3}$, defined by

$$\mathcal{G}^{m_1 m_2 m_3}_{l_1 l_2 l_3} \equiv \int d^2\hat{\mathbf{n}} Y_{l_1 m_1}(\hat{\mathbf{n}}) Y_{l_2 m_2}(\hat{\mathbf{n}}) Y_{l_3 m_3}(\hat{\mathbf{n}})$$
$$= \sqrt{\frac{(2l_1+1)(2l_2+1)(2l_3+1)}{4\pi}} \begin{pmatrix} l_1 & l_2 & l_3 \\ 0 & 0 & 0 \end{pmatrix} \begin{pmatrix} l_1 & l_2 & l_3 \\ m_1 & m_2 & m_3 \end{pmatrix}. \tag{4}$$

$\mathcal{G}^{m_1 m_2 m_3}_{l_1 l_2 l_3}$ is real, and satisfies all the conditions mentioned above.

Given the rotational invariance of the universe, $B_{l_1 l_2 l_3}$ is written as

$$B^{m_1 m_2 m_3}_{l_1 l_2 l_3} = \mathcal{G}^{m_1 m_2 m_3}_{l_1 l_2 l_3} b_{l_1 l_2 l_3}, \tag{5}$$

where $b_{l_1 l_2 l_3}$ is an arbitrary real symmetric function of l_1, l_2, and l_3. This form of equation (5) is necessary and sufficient to construct generic $B^{m_1 m_2 m_3}_{l_1 l_2 l_3}$ under the rotational invariance. Thus, we shall frequently use $b_{l_1 l_2 l_3}$ instead of $B^{m_1 m_2 m_3}_{l_1 l_2 l_3}$ in this paper, and call this function the "reduced" bispectrum, as $b_{l_1 l_2 l_3}$ contains all physical information in $B^{m_1 m_2 m_3}_{l_1 l_2 l_3}$. Since the reduced bispectrum does not contain the Wigner-3j symbol that merely ensures the triangle conditions and selection rules, it is easier to calculate and useful to quantify the physical properties of the bispectrum.

The observable quantity, the angle-averaged bispectrum $B_{l_1 l_2 l_3}$, is obtained by substituting equation (5) into (3),

$$B_{l_1 l_2 l_3} = \sqrt{\frac{(2l_1+1)(2l_2+1)(2l_3+1)}{4\pi}} \begin{pmatrix} l_1 & l_2 & l_3 \\ 0 & 0 & 0 \end{pmatrix} b_{l_1 l_2 l_3}, \tag{6}$$

where we have used the identity:

$$\sum_{m_1 m_2 m_3} \begin{pmatrix} l_1 & l_2 & l_3 \\ m_1 & m_2 & m_3 \end{pmatrix} \mathcal{G}^{m_1 m_2 m_3}_{l_1 l_2 l_3} = \sqrt{\frac{(2l_1+1)(2l_2+1)(2l_3+1)}{4\pi}} \begin{pmatrix} l_1 & l_2 & l_3 \\ 0 & 0 & 0 \end{pmatrix}. \tag{7}$$

Alternatively, one can define the bispectrum in the flat-sky approximation,

$$\langle a(\mathbf{l}_1) a(\mathbf{l}_1) a(\mathbf{l}_3) \rangle = (2\pi)^2 \delta^{(2)} (\mathbf{l}_1 + \mathbf{l}_2 + \mathbf{l}_3) B(\mathbf{l}_1, \mathbf{l}_2, \mathbf{l}_3), \tag{8}$$

where $\mathbf{l}$ is the two dimensional wave-vector on the sky. This definition of $B(\mathbf{l}_1, \mathbf{l}_2, \mathbf{l}_3)$ corresponds to equation (5), given the correspondence of $\mathcal{G}^{m_1 m_2 m_3}_{l_1 l_2 l_3} \to \delta^{(2)} (\mathbf{l}_1 + \mathbf{l}_2 + \mathbf{l}_3)$ in the flat-sky limit [23]. Thus,

$$b_{l_1 l_2 l_3} \approx B(\mathbf{l}_1, \mathbf{l}_2, \mathbf{l}_3) \qquad \text{(flat-sky approximation)}, \tag{9}$$

is satisfied. This fact also would motivate us to use the reduced bispectrum $b_{l_1 l_2 l_3}$ rather than the angular averaged bispectrum $B_{l_1 l_2 l_3}$. Note that $b_{l_1 l_2 l_3}$ is similar to $\hat{B}_{l_1 l_2 l_3}$ defined by Magueijo [18]. The relation is $b_{l_1 l_2 l_3} = \sqrt{4\pi} \hat{B}_{l_1 l_2 l_3}$.

III. PRIMARY BISPECTRUM AND SKEWNESS

A. Model of the primordial non-Gaussianity

If the primordial fluctuations are adiabatic scalar fluctuations, then

$$a_{lm} = 4\pi (-i)^l \int \frac{d^3 \mathbf{k}}{(2\pi)^3} \Phi(\mathbf{k}) g_{Tl}(k) Y^*_{lm}(\hat{\mathbf{k}}), \tag{10}$$

where $\Phi(\mathbf{k})$ is the primordial curvature perturbation in the Fourier space, and $g_{Tl}(k)$ is the radiation transfer function. a_{lm} thus takes over the non-Gaussianity, if any, from $\Phi(\mathbf{k})$. Although equation (10) is valid only if the universe is flat, it is straightforward to extend this to an arbitrary geometry. The isocurvature fluctuations can be similarly calculated by using the entropy perturbation and the proper transfer function.

In this paper, we explore the simplest weak non-linear coupling case:

$$\Phi(\mathbf{x}) = \Phi_L(\mathbf{x}) + f_{NL} \left(\Phi_L^2(\mathbf{x}) - \langle \Phi_L^2(\mathbf{x}) \rangle \right), \tag{11}$$

in real space, where $\Phi_L(\mathbf{x})$ denotes the linear gaussian part of the perturbation. $\langle \Phi(\mathbf{x}) \rangle = 0$ is guaranteed. Henceforth, we shall call f_{NL} the non-linear coupling constant. This model is based upon the slow-roll inflationary scenario. Salopek and Bond [11] and Gangui et al. [12] found that f_{NL} is given by a certain combination of the slope and the curvature of the inflaton potential. In the notation of Gangui et al., $\Phi_3 = 2f_{NL}$. Gangui et al. found that $\Phi_3 \sim 10^{-2}$ in the quadratic and the quartic inflaton potential models.

In the Fourier space, $\Phi(\mathbf{k})$ is decomposed into two parts:

$$\Phi(\mathbf{k}) = \Phi_L(\mathbf{k}) + \Phi_{NL}(\mathbf{k}), \tag{12}$$

and accordingly,

$$a_{lm} = a^L_{lm} + a^{NL}_{lm}, \tag{13}$$

where $\Phi_{NL}(\mathbf{k})$ is the non-linear part defined by

$$\Phi_{NL}(\mathbf{k}) \equiv f_{NL} \left[\int \frac{d^3 \mathbf{p}}{(2\pi)^3} \Phi_L(\mathbf{k}+\mathbf{p}) \Phi_L^*(\mathbf{p}) - (2\pi)^3 \delta^{(3)}(\mathbf{k}) \langle \Phi_L^2(\mathbf{x}) \rangle \right]. \tag{14}$$

One can confirm that $\langle \Phi(\mathbf{k}) \rangle = 0$ is satisfied. In this model, a non-vanishing component of the $\Phi(\mathbf{k})$-field bispectrum is

$$\langle \Phi_L(\mathbf{k}_1) \Phi_L(\mathbf{k}_2) \Phi_{NL}(\mathbf{k}_3) \rangle = 2(2\pi)^3 \delta^{(3)}(\mathbf{k}_1 + \mathbf{k}_2 + \mathbf{k}_3) f_{NL} P_\Phi(k_1) P_\Phi(k_2), \tag{15}$$

where $P_\Phi(k)$ is the linear power spectrum given by $\langle \Phi_L(\mathbf{k}_1) \Phi_L(\mathbf{k}_2) \rangle = (2\pi)^3 P_\Phi(k_1) \delta^{(3)}(\mathbf{k}_1 + \mathbf{k}_2)$. We have also used $\langle \Phi_L(\mathbf{k}+\mathbf{p}) \Phi_L^*(\mathbf{p}) \rangle = (2\pi)^3 P_\Phi(p) \delta^{(3)}(\mathbf{k})$, and $\langle \Phi_L^2(\mathbf{x}) \rangle = (2\pi)^{-3} \int d^3 k P_\Phi(k)$.

Substituting equation (10) into (2), using equation (15) for the $\Phi(\mathbf{k})$-field bispectrum, and then integrating over angles $\hat{\mathbf{k}}_1$, $\hat{\mathbf{k}}_3$, and $\hat{\mathbf{k}}_3$, we obtain the primary CMB angular bispectrum,

$$B_{l_1l_2l_3}^{m_1m_2m_3} = \left\langle a_{l_1m_1}^L a_{l_2m_2}^L a_{l_3m_3}^{NL} \right\rangle + \left\langle a_{l_1m_1}^L a_{l_2m_2}^{NL} a_{l_3m_3}^L \right\rangle + \left\langle a_{l_1m_1}^{NL} a_{l_2m_2}^L a_{l_3m_3}^L \right\rangle$$

$$= 2\mathcal{G}_{l_1l_2l_3}^{m_1m_2m_3} \int_0^\infty r^2 dr \left[b_{l_1}^L(r)b_{l_2}^L(r)b_{l_3}^{NL}(r) + b_{l_1}^L(r)b_{l_2}^{NL}(r)b_{l_3}^L(r) + b_{l_1}^{NL}(r)b_{l_2}^L(r)b_{l_3}^L(r) \right], \tag{16}$$

where

$$b_l^L(r) \equiv \frac{2}{\pi} \int_0^\infty k^2 dk P_\Phi(k) g_{Tl}(k) j_l(kr), \tag{17}$$

$$b_l^{NL}(r) \equiv \frac{2}{\pi} \int_0^\infty k^2 dk f_{NL} g_{Tl}(k) j_l(kr). \tag{18}$$

Note that $b_l^L(r)$ is a dimensionless quantity, while $b_l^{NL}(r)$ has a dimension of L^{-3}.

One confirms that the form of equation (5) holds. Thus, the reduced bispectrum, $b_{l_1l_2l_3} = B_{l_1l_2l_3}^{m_1m_2m_3} \left(\mathcal{G}_{l_1l_2l_3}^{m_1m_2m_3} \right)^{-1}$ (Eq.(5)), for the primordial non-Gaussianity is

$$b_{l_1l_2l_3}^{primary} = 2 \int_0^\infty r^2 dr \left[b_{l_1}^L(r)b_{l_2}^L(r)b_{l_3}^{NL}(r) + b_{l_1}^L(r)b_{l_2}^{NL}(r)b_{l_3}^L(r) + b_{l_1}^{NL}(r)b_{l_2}^L(r)b_{l_3}^L(r) \right]. \tag{19}$$

$b_{l_1l_2l_3}^{primary}$ is fully specified by a single constant parameter f_{NL}, as the cosmological parameters will be precisely determined by measuring the CMB angular power spectrum C_l (e.g., [24]). It should be stressed again that this is the special case in the slow-roll limit. If the slow-roll condition is not satisfied, then $f_{NL} = f_{NL}(k_1, k_2, k_3)$ at equation (15) [12]. Wang and Kamionkowski [25] have developed the formula to compute $B_{l_1l_2l_3}$ from the generic form of $\Phi(\mathbf{k})$-field bispectrum. Our formula (Eq.(16)) agrees with theirs, given our form of the $\Phi(\mathbf{k})$-field bispectrum (Eq.(15)).

Even if the inflation produced Gaussian fluctuations, Pyne and Carroll pointed out that the general relativistic second-order perturbation theory would produce terms of $f_{NL} \sim \mathcal{O}(1)$ [26]. For generic slow-roll models, these terms dominate the primary non-Gaussianity.
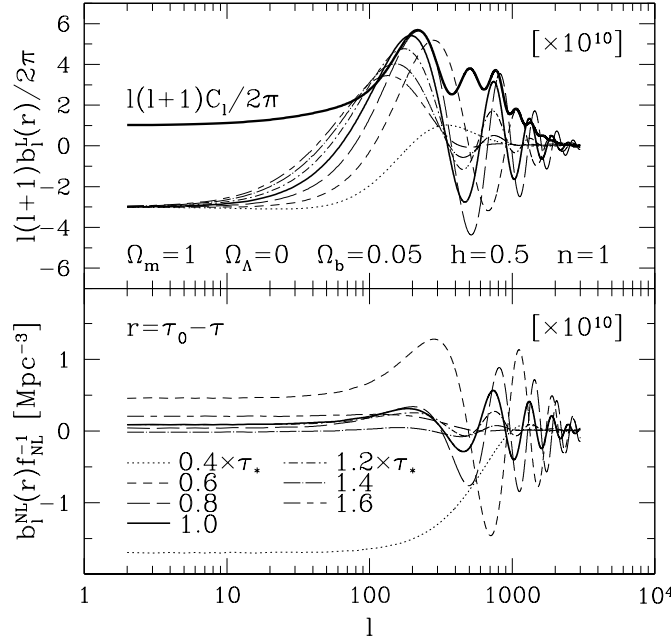

FIG. 1. This figure shows $b_l^L(r)$ (Eq.(17)) and $b_l^{NL}(r)$ (Eq.(18)), the two terms in our calculation of the primary CMB angular bispectrum, as a function of r. Various lines in the upper panel show $\left[l(l+1)b_l^L(r)/2\pi \right] \times 10^{10}$, where $r = c\,(\tau_0 - \tau)$, at $\tau = 0.4, 0.6, 0.8, 1.0, 1.2, 1.4,$ and $1.6 \times \tau_*$ (decoupling time), while $\left[b_l^{NL}(r) f_{NL}^{-1} \right] \times 10^{10}$ are shown in the lower panel. τ_0 is the present-day conformal time. Note that $c\tau_0 = 11.8$ Gpc, and $c\tau_* = 235$ Mpc in our cosmological model chosen here. The thickest solid line in the upper panel is the CMB angular power spectrum $[l(l+1)C_l/2\pi] \times 10^{10}$. C_l is shown for comparison.

4

B. Numerical results of the primary bispectrum

We evaluate the primary CMB bispectrum (Eqs.(16)–(19)) numerically. We compute the full radiation transfer function $g_{Tl}(k)$ with the CMBFAST [27] code, and assume the single power law spectrum, $P_\Phi(k) \propto k^{n-4}$, for the primordial curvature fluctuations. The integration over k (Eqs.(17) and (18)) is done by the algorithm used in CMBFAST. The cosmological model is the scale-invariant standard cold dark matter model with $\Omega_m = 1$, $\Omega_\Lambda = 0$, $\Omega_b = 0.05$, $h = 0.5$, and $n = 1$, and with the power spectrum $P_\Phi(k)$ normalized to COBE [28]. Although this model is almost excluded by current observations, it is still useful to depict the basic effects of the transfer function on the bispectrum.

Figure 1 shows $b_l^L(r)$ (Eq.(17)) and $b_l^{NL}(r)$ (Eq.(18)) for several different values of r. $r = c\,(\tau_0 - \tau)$, where τ is the conformal time, and τ_0 is at the present. In our model, $c\tau_0 = 11.8$ Gpc, and the decoupling epoch occurs at $c\tau_* = 235$ Mpc at which the differential visibility has a maximum. Our $c\tau_0$ includes the radiation effect on the expansion of universe, otherwise $c\tau_0 = 12.0$ Gpc. τ_* is the epoch when the most of the primary signal is generated. $b_l^L(r)$ and C_l look very similar one another in the shape and the amplitude at $l \gtrsim 100$, although the amplitude in the Sachs–Wolfe regime is different by a factor of -3. This is because C_l is proportional to $P_\Phi(k)g_{Tl}^2(k)$, while $b_l^L(r) \propto P_\Phi(k)g_{Tl}(k)$, where $g_{Tl} = -1/3$. $b_l^L(r)$ has a good phase coherence over wide range of r, while the phase of $b_l^{NL}(r)$ in high-l regime oscillates rapidly as a function of r. This strongly damps the integrated result of the bispectrum (Eq.(16)) in high-l regime. The main difference between C_l and $b_l(r)$ is that $b_l(r)$ changes a sign, while C_l does not.

Looking at figure 1, we find $l^2 b_l^L \sim 2 \times 10^{-9}$ and $b_l^{NL} f_{NL}^{-1} \sim 10^{-10}$ Mpc^{-3}. The most signal coming from the decoupling, the volume element at τ_* is $r_*^2 \Delta r_* \sim (10^4)^2 \times 10^2$ Mpc^3, and thus we estimate an order of magnitude of the primary reduced bispectrum (Eq.(19)) as

$$b_{lll}^{primary} \sim l^{-4} \left[2 r_*^2 \Delta r_* \left(l^2 b_l^L \right)^2 b_l^{NL} \times 3 \right] \sim l^{-4} \times 2 \times 10^{-17} f_{NL}. \tag{20}$$

Since $b_l^{NL} f_{NL}^{-1} \sim r_*^{-2} \delta(r - r_*)$ (see Eq.(23)), $r_*^2 \Delta r_* b_l^{NL} f_{NL}^{-1} \sim 1$. This rough estimate agrees with the numerical result below (figure 2).
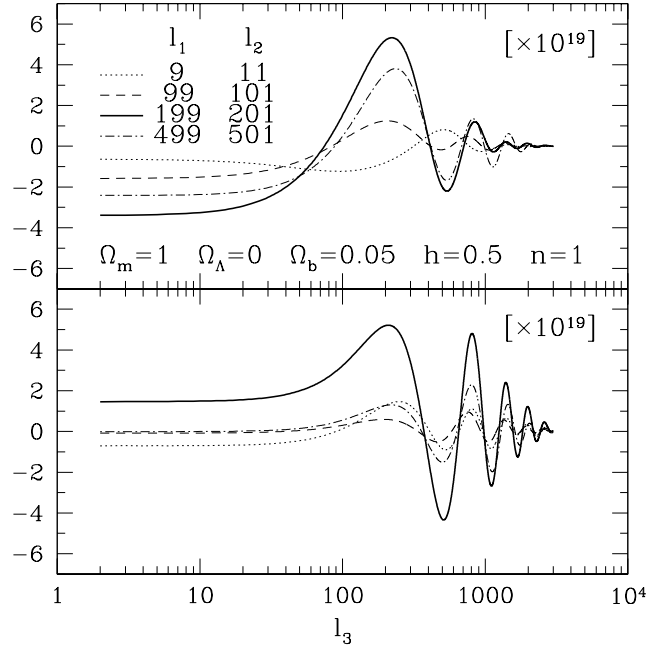

FIG. 2.   The primary CMB angular bispectrum (Eq.(16)) divided by the Gaunt integral $\mathcal{G}_{l_1 l_2 l_3}^{m_1 m_2 m_3}$ (Eq.(4)). The upper panel shows $\left[l_2(l_2+1)l_3(l_3+1) \left\langle a_{l_1 m_1}^{NL} a_{l_2 m_2}^{L} a_{l_3 m_3}^{L} \right\rangle f_{NL}^{-1} \left(\mathcal{G}_{l_1 l_2 l_3}^{m_1 m_2 m_3} \right)^{-1} /(2\pi)^2 \right] \times 10^{19}$, while the lower panel shows $\left[l_1(l_1+1)l_2(l_2+1) \left\langle a_{l_1 m_1}^{L} a_{l_2 m_2}^{L} a_{l_3 m_3}^{NL} \right\rangle f_{NL}^{-1} \left(\mathcal{G}_{l_1 l_2 l_3}^{m_1 m_2 m_3} \right)^{-1} /(2\pi)^2 \right] \times 10^{19}$. Those are shown as functions of l_3 for $(l_1, l_2) = (9, 11), (99, 101), (199, 201)$, and $(499, 501)$.

Figure 2 shows the integrated bispectrum (Eq.(16)) divided by the Gaunt integral $\mathcal{G}_{l_1l_2l_3}^{m_1m_2m_3}$, which is basically $b_{l_1l_2l_3}^{primary}$. Since the signal comes primarily from the decoupling epoch τ_* as mentioned above, the integration boundary is chosen as $c(\tau_0 - 2\tau_*) \le r \le c(\tau_0 - 0.1\tau_*)$. We use a step-size of $0.1c\tau_*$, as we found that a step size of $0.01c\tau_*$ gives very similar results. While the bispectrum is a 3-d function, we show different 1-d slices of the bispectrum in this figure. $l_2(l_2+1)l_3(l_3+1)\langle a_{l_1m_1}^{NL} a_{l_2m_2}^L a_{l_3m_3}^L\rangle (\mathcal{G}_{l_1l_2l_3}^{m_1m_2m_3})^{-1}/(2\pi)^2$ is plotted as a function of l_3 in the upper panel, while $l_1(l_1+1)l_2(l_2+1)\langle a_{l_1m_1}^L a_{l_2m_2}^L a_{l_3m_3}^{NL}\rangle (\mathcal{G}_{l_1l_2l_3}^{m_1m_2m_3})^{-1}/(2\pi)^2$ is plotted in the lower panel. $l(l+1)/(2\pi)$ is multiplied for each $b_l^L(r)$ which contains $P_\Phi(k)$ so as the Sachs–Wolfe plateau at $l_3 \lesssim 10$ is easily seen in figure 2. l_1 and l_2 are chosen so as $(l_1,l_2) = (9,11), (99,101), (199,201)$, and $(499,501)$. We find that the $(l_1,l_2) = (199,201)$ mode, the first acoustic peak mode, has the largest signal in this family of parameters. The upper panel has a prominent first acoustic peak, and strongly damped oscillations in high-l regime. The lower panel also has a first peak, but damps more slowly. The typical amplitude of the reduced bispectrum is $l^4 b_{lll}^{primary} f_{NL}^{-1} \sim 10^{-17}$, which agrees with an order of magnitude estimate (Eq.(20)).

Our formula (Eq.(19)) and numerical results agree with Gangui et al. [12] calculation in the Sachs–Wolfe regime, where $g_{Tl}(k) \approx -j_l(kr_*)/3$, and thus

$$b_{l_1l_2l_3}^{primary} \approx -6f_{NL}\left(C_{l_1}^{SW}C_{l_2}^{SW} + C_{l_1}^{SW}C_{l_3}^{SW} + C_{l_2}^{SW}C_{l_3}^{SW}\right) \qquad \text{(Sachs–Wolfe approximation)}. \tag{21}$$

Each term is in the same order as equation (19). C_l^{SW} is the CMB angular power spectrum in the Sachs–Wolfe approximation,

$$C_l^{SW} \equiv \frac{2}{9\pi}\int_0^\infty k^2 dk P_\Phi(k) j_l^2(kr_*). \tag{22}$$

In deriving equation (21) from (19), we approximated $b_l^{NL}(r)$ (Eq.(18)) to

$$b_l^{NL}(r) \approx \left(-\frac{f_{NL}}{3}\right)\frac{2}{\pi}\int_0^\infty k^2 dk j_l(kr_*) j_l(kr) = -\frac{f_{NL}}{3}r_*^{-2}\delta(r - r_*). \tag{23}$$

The Sachs–Wolfe approximation (Eq.(21)) is valid only when l_1, l_2, and l_3 are all less than ~ 10, where Gangui et al.'s formula gives $\sim -6 \times 10^{-20}$ in figure 2. It should be stressed again that the Sachs–Wolfe approximation gives the qualitatively different result from our full calculation (Eq.(19)) at $l_i \gtrsim 10$. The full bispectrum does change a sign, while the approximation never changes a sign because of the use of C_l^{SW}. The acoustic oscillation and the sign change are actually great advantages, when we try to separate the primary bispectrum from various secondary bispectra. We shall study this point later.

C. Primary skewness

The skewness S_3,

$$S_3 \equiv \left\langle \left(\frac{\Delta T(\hat{\mathbf{n}})}{T}\right)^3\right\rangle \tag{24}$$

is the simplest statistic characterizing the non-Gaussianity. S_3 is expanded in terms of $B_{l_1l_2l_3}$ (Eq.(3)) or $b_{l_1l_2l_3}$ (Eq.(5)) as

$$S_3 = \frac{1}{4\pi}\sum_{l_1l_2l_3}\sqrt{\frac{(2l_1+1)(2l_2+1)(2l_3+1)}{4\pi}}\begin{pmatrix} l_1 & l_2 & l_3 \\ 0 & 0 & 0\end{pmatrix} B_{l_1l_2l_3} W_{l_1}W_{l_2}W_{l_3}$$

$$= \frac{1}{2\pi^2}\sum_{2 \le l_1l_2l_3}\left(l_1+\frac{1}{2}\right)\left(l_2+\frac{1}{2}\right)\left(l_3+\frac{1}{2}\right)\begin{pmatrix} l_1 & l_2 & l_3 \\ 0 & 0 & 0\end{pmatrix}^2 b_{l_1l_2l_3}W_{l_1}W_{l_2}W_{l_3}, \tag{25}$$

where W_l is the experimental window function. We have used equation (6) to replace $B_{l_1l_2l_3}$ by the reduced bispectrum $b_{l_1l_2l_3}$ in the last equality. Since $l = 0$ and 1 modes are not observable, we have excluded them from the summation. Throughout this paper, we consider the single-beam window function, $W_l = e^{-l(l+1)/(2\sigma_b^2)}$, where $\sigma_b = \text{FWHM}/\sqrt{8\ln 2}$. Since $\begin{pmatrix} l_1 & l_2 & l_3 \\ 0 & 0 & 0\end{pmatrix}^2 b_{l_1l_2l_3}$ is symmetric under permutation of indices, it is useful to change the way of summation as

$$\sum_{2 \le l_1 l_2 l_3} \longrightarrow 6 \sum_{2 \le l_1 \le l_2 \le l_3} . \tag{26}$$

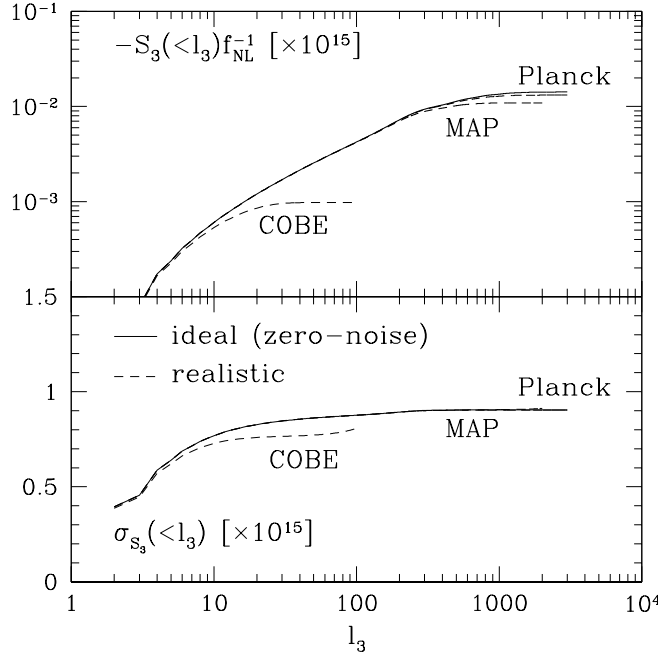Since this reduces the number of summations by a factor of $\simeq 6$, we shall use this convention henceforth.

FIG. 3. The upper panel shows the primary CMB skewness (Eq.(25)) summed up to a certain l_3, $-S_3(< l_3)f_{NL}^{-1} \times 10^{15}$. The lower panel shows the noise (Eq.(60)) summed up to l_3, $\sigma_{S_3}(< l_3) \times 10^{15}$. Solid line represents the zero-noise ideal experiment, while dotted lines show COBE, MAP, and Planck experiments.

The upper panel of figure 3 plots $S_3(< l_3)$, which is S_3 summed up to a certain l_3, for FWHM beam-sizes of $7°$, $13'$, and $5'.5$. These values correspond to beam-sizes of COBE, MAP, and Planck experiments, respectively. Figure 3 also plots the infinitesimal thin-beam case. MAP, Planck, and the ideal experiments measure very similar S_3 one another, despite the fact that Planck and the ideal experiments can use much more number of modes than MAP. The reason is as follows. Looking at equation (25), one finds that S_3 is the linear integration of $b_{l_1 l_2 l_3}$ over l_i. Thus, integrating oscillations in $b_{l_1 l_2 l_3}^{primary}$ around zero (see figure 2) damps the non-Gaussian signal in small angular scales, $l \gtrsim 300$. Since the COBE scale is basically dominated by the Sachs–Wolfe effect, no oscillation, the cancellation affects S_3 less significantly than in MAP and Planck scales, while Planck suffers from severe cancellation in small angular scales. Even Planck and the ideal experiments measure the same amount of S_3 as MAP does. As a result, measured S_3 almost saturates at the MAP resolution scale, $l \sim 500$.

We conclude this section by noting that when we can calculate the expected form of the bispectrum, then it is a "matched filter" for detecting the non-Gaussianity in the data, and thus much more powerful tool than the skewness in which the information is lost through the coarse-graining.

IV. SECONDARY SOURCES OF THE CMB BISPECTRUM

Even if the CMB bispectrum were significantly detected in the CMB map, the origin would not necessarily be primordial, but rather would be various foregrounds such as the Sunyaev–Zel'dovich effect [29] (hereafter SZ), the weak lensing effect, extragalactic radio sources, and so on. In order to isolate the primordial origin from others, we have to know the accurate form of bispectra produced by the foregrounds.

A. Coupling between the weak lensing and the Sunyaev–Zel'dovich effects

The coupling between the SZ and the weak lensing effects would produce an observable effect in the bispectrum [21,22]. The CMB temperature field including the SZ and the lensing effects is expanded as

$$\frac{\Delta T(\hat{\mathbf{n}})}{T} = \frac{\Delta T^P(\hat{\mathbf{n}} + \nabla\Theta(\hat{\mathbf{n}}))}{T} + \frac{\Delta T^{SZ}(\hat{\mathbf{n}})}{T} \approx \frac{\Delta T^P(\hat{\mathbf{n}})}{T} + \nabla\left(\frac{\Delta T^P(\hat{\mathbf{n}})}{T}\right) \cdot \nabla\Theta(\hat{\mathbf{n}}) + \frac{\Delta T^{SZ}(\hat{\mathbf{n}})}{T}, \tag{27}$$

where P denotes the primary anisotropy, $\Theta(\hat{\mathbf{n}})$ is the lensing potential:

$$\Theta(\hat{\mathbf{n}}) \equiv -2\int_0^{r_*} dr \frac{r_* - r}{rr_*} \Phi(r, \hat{\mathbf{n}}r), \tag{28}$$

and SZ denotes the SZ effect:

$$\frac{\Delta T^{SZ}(\hat{\mathbf{n}})}{T} = y(\hat{\mathbf{n}})j_\nu, \tag{29}$$

where j_ν is the spectral function of the SZ effect [29]. $y(\hat{\mathbf{n}})$ is the Compton y-parameter given by

$$y(\hat{\mathbf{n}}) \equiv y_0 \int \frac{dr}{r_*} \frac{T_\rho(r, \hat{\mathbf{n}}r)}{\overline{T}_{\rho0}} a^{-2}(r), \tag{30}$$

where

$$y_0 \equiv \frac{\sigma_T \overline{\rho}_{gas0} k_B \overline{T}_{\rho0} r_*}{\mu_e m_p m_e c^2} = 4.3 \times 10^{-4} \mu_e^{-1} \left(\Omega_b h^2\right) \left(\frac{k_B \overline{T}_{\rho0}}{1\text{ keV}}\right) \left(\frac{r_*}{10\text{ Gpc}}\right). \tag{31}$$

$T_\rho \equiv \rho_{gas} T_e / \overline{\rho}_{gas}$ is the electron temperature weighted by the gas mass density, the overline denotes the volume average, and the subscript 0 means the present epoch. We adopt $\mu_e^{-1} = 0.88$, where $\mu_e^{-1} \equiv n_e/(\rho_{gas}/m_p)$ is the number of electrons per proton mass in fully ionized medium. Other quantities have their usual meanings.

Transforming equation (27) into harmonic space,

$$a_{lm} = a_{lm}^P + \sum_{l'm'}\sum_{l''m''}(-1)^m \mathcal{G}_{ll'l''}^{-mm'm''}\frac{l'(l'+1) - l(l+1) + l''(l''+1)}{2}a_{l'm'}^P \Theta_{l''m''} + a_{lm}^{SZ}$$

$$= a_{lm}^P + \sum_{l'm'}\sum_{l''m''}(-1)^{m+m'+m''}\mathcal{G}_{ll'l''}^{-mm'm''}\frac{l'(l'+1) - l(l+1) + l''(l''+1)}{2}a_{l'-m'}^{P*}\Theta_{l''-m''}^* + a_{lm}^{SZ}, \tag{32}$$

where $\mathcal{G}_{l_1 l_2 l_3}^{m_1 m_2 m_3}$ is the Gaunt integral (Eq.(4)). Substituting equation (32) into (2), and using the identity $\mathcal{G}_{l_1 l_2 l_3}^{-m_1 -m_2 -m_3} = \mathcal{G}_{l_1 l_2 l_3}^{m_1 m_2 m_3}$, we obtain the bispectrum,

$$B_{l_1 l_2 l_3}^{m_1 m_2 m_3} = \mathcal{G}_{l_1 l_2 l_3}^{m_1 m_2 m_3}\left[\frac{l_1(l_1+1) - l_2(l_2+1) + l_3(l_3+1)}{2}C_{l_1}^P\left\langle\Theta_{l_3 m_3}^* a_{l_3 m_3}^{SZ}\right\rangle + 5\text{ permutations}\right]. \tag{33}$$

The form of equation (5) is confirmed, and then the reduced bispectrum $b_{l_1 l_2 l_3}^{sz-lens}$ includes terms in the square bracket.

The cross-correlation power spectrum of the lensing and the SZ effects, $\left\langle\Theta_{lm}^* a_{lm}^{SZ}\right\rangle$, appearing in equation (33) was first derived by Goldberg and Spergel [21]. They assumed the linear pressure bias model proposed by Persi et al. [30]: $T_\rho = \overline{T}_\rho b_{gas}\delta$, and the mean temperature evolution of $\overline{T}_\rho \simeq \overline{T}_{\rho0}(1+z)^{-1}$ for $z < 2$ as roughly suggested by recent hydrodynamic simulations [31–33]. Then they derived

$$\left\langle\Theta_{lm}^* a_{lm}^{SZ}\right\rangle \simeq -j_\nu \frac{4y_0 b_{gas} l^2}{3\Omega_m H_0^2}\int_0^{z_*} dz \frac{dr}{dz} D^2(z)(1+z)^2 \frac{r_* - r(z)}{r_*^2 r^5(z)}P_\Phi\left(k = \frac{l}{r(z)}\right), \tag{34}$$

where $D(z)$ is the linear growth factor. Simulations without non-gravitational heating [32,33] suggest that $\overline{T}_{\rho0} \sim 0.2 - 0.4$ keV and $b_{gas} \sim 5 - 10$, and similar numbers are obtained by analytic estimations [32,34]. In this pressure bias model, free parameters except cosmological parameters are $\overline{T}_{\rho0}$ and b_{gas}. However, both actually depend on cosmological models [32]. Since $l^3\left\langle\Theta_{lm}^* a_{lm}^{SZ}\right\rangle \sim 2 \times 10^{-10}j_\nu \overline{T}_{\rho0}b_{gas}$ [21,22] and $l^2 C_l^P \sim 6 \times 10^{-10}$,

$$b_{lll}^{sz-lens} \sim l^{-3} \left[\left(l^2 C_l^P \right) \left(l^3 \left\langle \Theta_{lm}^* a_{lm}^{SZ} \right\rangle \right) \times 5/2 \right] \sim l^{-3} \times 3 \times 10^{-19} j_\nu \overline{T}_{\rho 0} b_{gas}, \tag{35}$$

where $\overline{T}_{\rho 0}$ is in units of 1 keV, and $b_{l_1 l_2 l_3} = B_{l_1 l_2 l_3}^{m_1 m_2 m_3} \left(\mathcal{G}_{l_1 l_2 l_3}^{m_1 m_2 m_3} \right)^{-1}$ (Eq.(5)) is the reduced bispectrum. Thus, comparing this to equation (20), we obtain

$$\frac{b_{lll}^{primary}}{b_{lll}^{sz-lens}} \sim l^{-1} \times 10 \left(\frac{f_{NL}}{j_\nu \overline{T}_{\rho 0} b_{gas}} \right). \tag{36}$$

This estimate suggests that the primary bispectrum is overwhelmed by the SZ–lensing bispectrum in small angular scales. This is why we have to separate the primary from the SZ–lensing effect.

B. Extragalactic radio and infrared sources

The bispectrum from extragalactic radio and infrared sources whose fluxes F are less than a certain detection threshold F_d is relatively simple to estimate, when they are assumed to be Poisson distributed. Since the Poisson distribution has the white noise spectrum, the reduced bispectrum (Eq.(5)) is constant, $b_{l_1 l_2 l_3}^{ps} = b^{ps} =$ constant, then we obtain

$$B_{l_1 l_2 l_3}^{m_1 m_2 m_3} = \mathcal{G}_{l_1 l_2 l_3}^{m_1 m_2 m_3} b^{ps}, \tag{37}$$

where

$$b^{ps}(< F_d) \equiv g^3(x) \int_0^{F_d} dF F^3 \frac{dn}{dF} = g^3(x) \frac{n(> F_d)}{3 - \beta} F_d^3. \tag{38}$$

The assumption of the Poisson distribution is fairly good approximation as found by Toffolatti et al. [35]. dn/dF is the differential source count per unit solid angle, and $n(> F_d) \equiv \int_{F_d}^\infty dF(dn/dF)$. The power law count, $dn/dF \propto F^{-\beta-1}$ with $\beta < 2$, has been assumed. $x \equiv h\nu/k_B T \simeq (\nu/56.80 \text{ GHz})(T/2.726 \text{ K})^{-1}$, and

$$g(x) \equiv 2 \frac{(hc)^2}{(k_B T)^3} \left(\frac{\sinh x/2}{x^2} \right)^2 \simeq \frac{1}{67.55 \text{ MJy sr}^{-1}} \left(\frac{T}{2.726 \text{ K}} \right)^{-3} \left(\frac{\sinh x/2}{x^2} \right)^2. \tag{39}$$

b^{ps} is otherwise written in terms of the Poisson angular power spectrum C^{ps}:

$$C^{ps}(< F_d) \equiv g^2(x) \int_0^{F_d} dF F^2 \frac{dn}{dF} = g^2(x) \frac{n(> F_d)}{2 - \beta} F_d^2, \tag{40}$$

as

$$b^{ps}(< F_d) = \frac{(2 - \beta)^{3/2}}{3 - \beta} \left[n(> F_d) \right]^{-1/2} \left[C^{ps}(< F_d) \right]^{3/2}. \tag{41}$$

Toffolatti et al. [35] estimated $n(> F_d) \sim 300 \text{ sr}^{-1}$ for $F_d \sim 0.2$ Jy at 217 GHz. This F_d corresponds to 5σ detection threshold for Planck experiment at 217 GHz. Refregier, Spergel and Herbig [36] extrapolated Toffolatti et al.'s estimation to 94 GHz, and obtained $n(> F_d) \sim 7 \text{ sr}^{-1}$ for $F_d \sim 2$ Jy, which corresponds to MAP 5σ threshold. These values yield

$$C^{ps}(90 \text{ GHz}, < 2 \text{ Jy}) \sim 2 \times 10^{-16}, \tag{42}$$
$$C^{ps}(217 \text{ GHz}, < 0.2 \text{ Jy}) \sim 1 \times 10^{-17}. \tag{43}$$

Thus, rough estimates for b^{ps} are

$$b^{ps}(90 \text{ GHz}, < 2 \text{ Jy}) \sim 2 \times 10^{-25}, \tag{44}$$
$$b^{ps}(217 \text{ GHz}, < 0.2 \text{ Jy}) \sim 5 \times 10^{-28}. \tag{45}$$

While we assumed the Euclidean source count ($\beta = 3/2$) here for definiteness, this does not affect an order of magnitude estimates above. Since the primary reduced bispectrum $\propto l^{-4}$ (Eq.(20)) and the SZ–lensing reduced bispectrum $\propto l^{-3}$ (Eq.(35)), the Poisson bispectrum rapidly becomes to dominate the total bispectrum in small angular scales,

$$\frac{b_{lll}^{primary}}{b^{ps}} \sim l^{-4} \times 10^7 \left(\frac{f_{NL}}{b^{ps}/10^{-25}} \right), \tag{46}$$

$$\frac{b_{lll}^{sz-lens}}{b^{ps}} \sim l^{-3} \times 10^6 \left(\frac{j_\nu \overline{T}_{\rho 0} b_{gas}}{b^{ps}/10^{-25}} \right). \tag{47}$$

For example, the SZ–lensing bispectrum measured by MAP experiment is overwhelmed by point sources at $l \gtrsim 100$.

V. MEASURING BISPECTRA

A. Fisher matrix

We shall discuss the detectability of CMB experiments to the primary non-Gaussianity in the bispectrum. We also need to separate it from secondary bispectra. Suppose that we try to fit the observed bispectrum $B^{obs}_{l_1 l_2 l_3}$ by theoretically calculated bispectra which include both primary and secondary sources. Then we minimize χ^2 defined by

$$\chi^2 \equiv \sum_{2 \leq l_1 \leq l_2 \leq l_3} \frac{\left(B^{obs}_{l_1 l_2 l_3} - \sum_i A_i B^{(i)}_{l_1 l_2 l_3} \right)^2}{\sigma^2_{l_1 l_2 l_3}}, \tag{48}$$

where i denotes a component such as the primary, the SZ and lensing effects, extragalactic sources, and so on. Unobservable modes $l = 0$ and 1 are removed. In case that the non-Gaussianity is small, the cosmic variance of the bispectrum is given by the six-point function of a_{lm} [37,38]. The variance of $B_{l_1 l_2 l_3}$ is then calculated as [20,39]

$$\sigma^2_{l_1 l_2 l_3} \equiv \left\langle B^2_{l_1 l_2 l_3} \right\rangle - \left\langle B_{l_1 l_2 l_3} \right\rangle^2 \approx \mathcal{C}_{l_1} \mathcal{C}_{l_2} \mathcal{C}_{l_3} \Delta_{l_1 l_2 l_3}, \tag{49}$$

where $\Delta_{l_1 l_2 l_3}$ takes values 1, 2, and 6 for cases of that all l's are different, two of them are same, and all are same, respectively. $\mathcal{C}_l \equiv C_l + C^N_l$ is the total CMB angular power spectrum, which includes the power spectrum of the detector noise C^N_l. C^N_l is calculated analytically using the formula derived by Knox [40] with the noise characteristics of the relevant experiments. We do not include C_l from secondary sources, as they are totally subdominant compared with the primary C_l and C^N_l for relevant experiments. For example, inclusion of C_l from extragalactic sources (Eqs.(42) or (43)) changes our results less than 10%.

Taking $\partial \chi^2 / \partial A_i = 0$, we obtain the normal equation,

$$\sum_j \left[\sum_{2 \leq l_1 \leq l_2 \leq l_3} \frac{B^{(i)}_{l_1 l_2 l_3} B^{(j)}_{l_1 l_2 l_3}}{\sigma^2_{l_1 l_2 l_3}} \right] A_j = \sum_{2 \leq l_1 \leq l_2 \leq l_3} \frac{B^{obs}_{l_1 l_2 l_3} B^{(i)}_{l_1 l_2 l_3}}{\sigma^2_{l_1 l_2 l_3}}. \tag{50}$$

Thus, we define the Fisher matrix F_{ij} as

$$F_{ij} \equiv \sum_{2 \leq l_1 \leq l_2 \leq l_3} \frac{B^{(i)}_{l_1 l_2 l_3} B^{(j)}_{l_1 l_2 l_3}}{\sigma^2_{l_1 l_2 l_3}} = \frac{2}{\pi} \sum_{2 \leq l_1 \leq l_2 \leq l_3} \left(l_1 + \frac{1}{2} \right) \left(l_2 + \frac{1}{2} \right) \left(l_3 + \frac{1}{2} \right) \begin{pmatrix} l_1 & l_2 & l_3 \\ 0 & 0 & 0 \end{pmatrix}^2 \frac{b^{(i)}_{l_1 l_2 l_3} b^{(j)}_{l_1 l_2 l_3}}{\sigma^2_{l_1 l_2 l_3}}, \tag{51}$$

where we have used equation (6) to replace $B_{l_1 l_2 l_3}$ by the reduced bispectrum $b_{l_1 l_2 l_3}$ (see Eq.(5) for definition). Since the covariance matrix of A_i is F^{-1}_{ij}, we define the signal-to-noise ratio $(S/N)_i$ for a component i, the correlation coefficient r_{ij} between different components i and j, and the degradation parameter d_i of $(S/N)_i$ due to r_{ij} as

$$\left(\frac{S}{N} \right)_i \equiv \frac{1}{\sqrt{F^{-1}_{ii}}}, \tag{52}$$

$$r_{ij} \equiv \frac{F^{-1}_{ij}}{\sqrt{F^{-1}_{ii} F^{-1}_{jj}}}, \tag{53}$$

$$d_i \equiv F_{ii} F^{-1}_{ii}. \tag{54}$$

Note that r_{ij} does not depend on amplitudes of bispectra, but shapes. d_i is defined so as $d_i = 1$ for zero degradation, while $d_i > 1$ for degraded $(S/N)_i$. Spergel and Goldberg [20] and Cooray and Hu [22] considered the diagonal component of F^{-1}_{ij}, while we study all components in order to discuss the separatability between various bispectra.

An order of magnitude estimation of S/N as a function of a certain angular resolution l is possible as follows. Since the number of modes contributing to S/N increases as $l^{3/2}$ and $l^3 \begin{pmatrix} l & l & l \\ 0 & 0 & 0 \end{pmatrix}^2 \sim 0.36 \times l$, we estimate $(S/N)_i \sim (F_{ii})^{1/2}$ as

$$\left(\frac{S}{N} \right)_i \sim \frac{1}{3\pi} l^{3/2} \times l^{3/2} \left| \begin{pmatrix} l & l & l \\ 0 & 0 & 0 \end{pmatrix} \right| \times \frac{l^3 b^{(i)}_{lll}}{(l^2 C_l)^{3/2}} \sim l^5 b^{(i)}_{lll} \times 4 \times 10^{12}, \tag{55}$$

where we have used $l^2 C_l \sim 6 \times 10^{-10}$.

Table I and II tabulate all components of F_{ij} and F_{ij}^{-1}, respectively. Table III summarizes $(S/N)_i$, while table IV tabulates d_i in the diagonal, and r_{ij} in the off-diagonal parts.

B. Measuring primary bispectrum

Figure 4 shows the numerical results of differential S/N for the primary bispectrum at $\ln l_3$ interval, $\left[d(S/N)^2/d \ln l_3 \right]^{1/2} f_{NL}^{-1}$, in the upper panel, and $(S/N)(< l_3) f_{NL}^{-1}$, which is S/N summed up to a certain l_3, in the lower panel. The detector noises C_l^N have been computed for COBE 4-yr map [41], for MAP 90 GHz channel, and for Planck 217 GHz channel, but the effect of limited sky coverage is neglected. Figure 4 also shows results for the ideal experiment with no noise: $C_l^N = 0$. Both $\left[d(S/N)^2/d \ln l_3 \right]^{1/2}$ and $(S/N)(< l_3)$ are monotonically increasing function with l_3 as roughly $\propto l_3$ up to $l_3 \sim 2000$ for the ideal experiment.

Beyond $l_3 \sim 2000$, an enhancement of the damping tail in C_l because of the weak lensing effect [42] stops $\left[d(S/N)^2/d \ln l_3 \right]^{1/2}$ and then $(S/N)(< l_3)$ increasing. This leads to an important constraint on the observation; even for the ideal noise-free and the infinitesimal thin-beam experiment, there is an upper limit on the value of $S/N \lesssim 0.3 f_{NL}$. For a given realistic experiment, $\left[d(S/N)^2/d \ln l_3 \right]^{1/2}$ has a maximum at a scale near the beam-size.
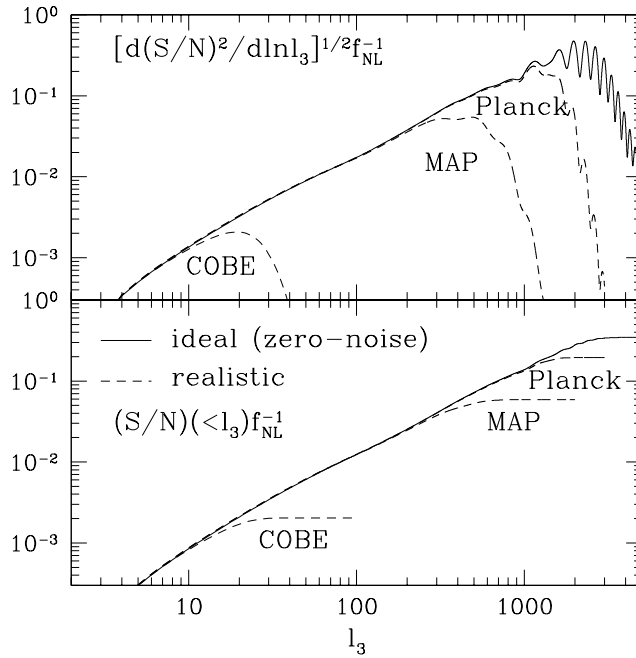

FIG. 4. The predictions of the signal-to-noise ratio, S/N, for COBE, MAP, and Planck experiments (see Eq.(52)). The differential S/N at $\ln l_3$ interval is shown in the upper panel, while the cumulative S/N up to a certain l_3 is shown in the lower panel. Both are in units of f_{NL}. Solid line represents the zero-noise ideal experiment, while dotted lines show the realistic experiments mentioned above. The total $(S/N) f_{NL}^{-1}$ are 1.7×10^{-3}, 5.8×10^{-2}, and 0.19 for COBE, MAP, and Planck experiments, respectively.

The total $(S/N) f_{NL}^{-1}$ are 1.7×10^{-3}, 5.8×10^{-2}, and 0.19 for COBE, MAP and Planck experiments, respectively (see table III). In order to obtain $S/N > 1$, therefore, we need $f_{NL} > 600, 20$, and 5 for each corresponding experiment, while the ideal experiment requires $f_{NL} > 3$ (see table V). These values are also roughly obtained by substituting equation (20) into (55),

$$\left(\frac{S}{N} \right)_{primary} \sim l \times 10^{-4} f_{NL}. \tag{56}$$

The degradation parameters $d_{primary}$ are 1.46, 1.01, and 1.00 for COBE, MAP, and Planck experiments, respectively (see table IV). This means that MAP and Planck experiments will separate the primary bispectrum from others at 1%

11

or better accuracies. Since the primary and other secondary sources change monotonically in the COBE angular scales, COBE cannot discriminate between them very well. In the MAP and Planck scales, however, the primary bispectrum starts oscillating around zero, and then is well separated in shape from other secondaries, as the secondaries do not oscillate. This is good news for the forthcoming high angular resolution CMB experiments.

C. Measuring secondary bispectra

The signal-to-noises for measuring the SZ–lensing bispectrum $(S/N)_{sz-lens}$ in units of $|j_\nu|\overline{T}_{\rho0}b_{gas}$ are 1.8×10^{-4}, 0.34, and 6.2 for COBE, MAP, and Planck experiments, respectively (see table III). $\overline{T}_{\rho0}$ is in units of 1 keV. Using equations (55) and (35), we roughly estimate $(S/N)_{sz-lens}$ as

$$\left(\frac{S}{N}\right)_{sz-lens} \sim l^2 \times 10^{-6} |j_\nu|\overline{T}_{\rho0}b_{gas}. \tag{57}$$

Thus, $(S/N)_{sz-lens}$ increases with the angular resolution more rapidly than the primary bispectrum (see Eq.(56)). Since $|j_\nu|\overline{T}_{\rho0}b_{gas}$ should be an order of unity, COBE and MAP would not be expected to detect the SZ–lensing bispectrum; however, Planck would be sensitive enough to detect, depending on the frequency, i.e., a value of j_ν. For example, 217 GHz is totally insensitive to the SZ effect as $j_\nu \sim 0$, while $j_\nu = -2$ in the Rayleigh–Jeans regime.

The degradation parameters $d_{sz-lens}$ are 3.89, 1.16, and 1.00 for COBE, MAP, and Planck experiments, respectively (see table IV). Thus, Planck will separate the SZ–lensing bispectrum from other effects. Note that $(S/N)_{sz-lens}$ values must be an order of magnitude estimation, as our cosmological model is the COBE normalized SCDM yielding $\sigma_8 = 1.2$. Since this σ_8 is about a factor of 2 greater than the cluster normalization with $\Omega_m = 1$, and 20% greater than the normalization with $\Omega_m = 0.3$ [43]. Thus, this factor tends to overestimate $\langle\Theta_{lm}^* a_{lm}^{SZ}\rangle$ (Eq.(34)) by a factor of several. On the other hand, using the linear power spectrum for $P_\Phi(k)$ rather than the non-linear power spectrum tends to underestimate the effect by a factor of several at $l \sim 3000$ [22]. However, our main goal is to discriminate between shapes of various bispectra, not amplitudes, so that this factor does not affect our conclusion on the degradation parameters d_i.

For the extragalactic radio and infrared sources, we estimated the signal-to-noises as $5.7 \times 10^{-7}(b^{ps}/10^{-25})$, $2.2(b^{ps}/10^{-25})$, and $52(b^{ps}/10^{-27})$ for COBE, MAP, and Planck experiments, respectively (see table III), and the degradation parameters d_{ps} are 3.45, 1.14, and 1.00 (see table IV). Since

$$\left(\frac{S}{N}\right)_{ps} \sim l^5 \times 10^{-13} \left(\frac{b^{ps}}{10^{-25}}\right), \tag{58}$$

from equation (55), S/N of the bispectrum from point sources increases very rapidly with the angular resolution. Our estimate that MAP will detect the bispectrum from point sources is consistent with the results found by Refregier, Spergel and Herbig [36]. Although MAP cannot separate the Poisson bispectrum from the SZ–lensing bispectrum very well (see r_{ij} in table IV), it would not matter as the SZ–lensing bispectrum would be too small to be measured by MAP. Planck will do an excellent job on separating all kinds of bispectra, at least including the primary signal, SZ–lensing coupling, and extragalactic point sources, on the basis of the shape difference.

D. Measuring primary skewness

For the skewness, we define S/N as

$$\left(\frac{S}{N}\right)^2 \equiv \frac{S_3^2}{\sigma_{S_3}^2}, \tag{59}$$

where the variance is [44]

$$\sigma_{S_3}^2 \equiv \left\langle (S_3)^2 \right\rangle = 6 \int_{-1}^{1} \frac{d\cos\theta}{2} \left[\mathcal{C}(\theta)\right]^3$$

$$= 6 \sum_{l_1 l_2 l_3} \frac{(2l_1+1)(2l_2+1)(2l_3+1)}{(4\pi)^3} \begin{pmatrix} l_1 & l_2 & l_3 \\ 0 & 0 & 0 \end{pmatrix}^2 \mathcal{C}_{l_1}\mathcal{C}_{l_2}\mathcal{C}_{l_3}W_{l_1}^2 W_{l_2}^2 W_{l_3}^2$$

$$= \frac{9}{2\pi^3} \sum_{2 \le l_1 \le l_2 \le l_3} \left(l_1+\frac{1}{2}\right)\left(l_2+\frac{1}{2}\right)\left(l_3+\frac{1}{2}\right)\begin{pmatrix} l_1 & l_2 & l_3 \\ 0 & 0 & 0 \end{pmatrix}^2 \mathcal{C}_{l_1}\mathcal{C}_{l_2}\mathcal{C}_{l_3}W_{l_1}^2 W_{l_2}^2 W_{l_3}^2. \tag{60}$$

In the last equality, we have used the symmetry of summed quantity with respect to indices (Eq.(26)), and removed unobservable modes $l = 0$ and 1. Typically $\sigma_{S_3} \sim 10^{-15}$, as $\sigma_{S_3} \sim [\mathcal{C}(0)]^{3/2} \sim 10^{-15}$, where $\mathcal{C}(\theta)$ is the temperature auto correlation function including noise. The lower panel of figure 3 shows $\sigma_{S_3}(< l_3)$, which is $\sigma_{S_3}(< l_3)$ summed up to a certain l_3, for COBE, MAP, and Planck experiments as well as the ideal experiment. Since $\mathcal{C}_l W_l^2 = C_l e^{-l(l+1)\sigma_b^2} + w^{-1}$, where w^{-1} determines the white noise power spectrum of the detector noise according to the Knox's formula [40], the dominance of second term beyond the experimental angular resolution scale, $l \sim \sigma_b^{-1}$, keeps $\sigma_{S_3}(< l_3)$ slightly increasing with l_3, while $S_3(< l_3)$ becomes constant beyond that (see the upper panel of figure 3). As a result, S/N starts somewhat decreasing beyond the resolution. We use the maximum S/N for estimating the minimum value of f_{NL} needed to detect the primary S_3. We find that $f_{NL} > 800$, 80, 70, and 60 for COBE, MAP, Planck, and the ideal experiments, respectively, with all-sky coverage.

These f_{NL} values are systematically larger than those needed to detect $B_{l_1 l_2 l_3}$ by a factor of 1.3, 4, 14, and 20, respectively (see table V). Higher the angular resolution, less sensitive measuring the primary S_3 than $B_{l_1 l_2 l_3}$. This is because the cancellation effect in smaller angular scales due to the oscillation of $B_{l_1 l_2 l_3}$ damps S_3.
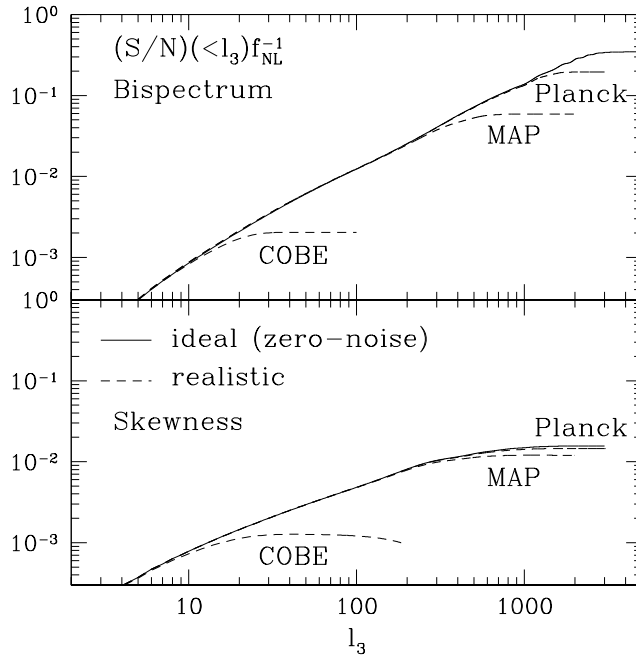

FIG. 5. The comparison of the signal-to-noise ratio summed up to a certain l_3, $S/N(< l_3)$, for the detection of the bispectrum (upper panel; Eq.(52)) and the skewness (lower panel; Eq.(59)) in units of f_{NL} for COBE, MAP, and Planck experiments (dotted lines), and the ideal experiment (solid line). See table V for values of f_{NL} in order to obtain $S/N > 1$.

VI. DISCUSSION AND CONCLUSION

Using the full radiation transfer function , we have computed numerically the primary cosmic microwave background bispectrum (Eq.(16)) and skewness (Eq.(25)) down to arcminutes angular scales. The primary bispectrum oscillates around zero (figure 2), thus the primary skewness saturates at the MAP angular resolution scale, $l \sim 500$ (figure 3). We have introduced the "reduced" bispectrum defined by equation (5), and confirmed that this quantity is more useful to describe the physical property of the bispectrum than the full bispectrum (Eq.(2)).

Figure 5 compares the expected signal-to-noise ratio for detecting the primary non-Gaussianity based on the bispectrum (Eq.(52)) to that based on the skewness (Eq.(59)). It shows that the bispectrum is almost an order of magnitude more sensitive to the non-Gaussianity than the skewness. We conclude that when we can compute the predicted form of the bispectrum, it becomes a "matched filter" for detecting the non-Gaussianity in the data, and thus much more powerful tool than the skewness. Table V summarizes f_{NL} required for detecting the primary non-Gaussianity using the bispectrum or the skewness with COBE, MAP, Planck, and the ideal experiments. This shows that even the ideal experiment needs $f_{NL} > 3$ in order to detect the primary bispectrum.

We estimated the secondary bispectra from the coupling between the Sunyaev–Zel'dovich (SZ) and the weak lensing effects, and from the extragalactic radio and infrared sources. Only Planck will detect the SZ–lensing bispectrum, while both MAP and Planck will detect the bispectrum from extragalactic point sources (table III).

We also studied how well we can discriminate among the primary, the SZ–lensing coupling, and the extragalactic point sources bispectra. We found that MAP and Planck will separate the primary from other secondary sources at 1% or better accuracies. This conclusion is due to the presence of acoustic oscillation in the primary bispectrum that does not appear in the secondary bispectra. The SZ–lensing coupling and the extragalactic sources are well separately measured by Planck experiment, although COBE and MAP cannot discriminate between them (table IV).

Our arguments about the ability to discriminate among various bispectra were fully based upon the shape difference, and thus did not take into account the spectral difference in the frequency space. As pointed out by [45,46], the multi-band observation is so efficient to discriminate among the primary signal and the other foreground contaminants for measuring the CMB anisotropy power spectrum. Their scheme should be effective on the bispectrum as well, and the accuracy of the foreground removal will be improved further. Thus, we expect that MAP and Planck will measure the primary bispectrum separately from the foregrounds.

The simplest inflationary scenario usually predicts small f_{NL} ($\sim 10^{-2}$) [11,12], and the second order perturbation theory yields $f_{NL} \sim 1$ [26]. Thus, the significant detection of the primary bispectrum or the skewness with any experiments means that the simplest inflationary scenario needs to be modified. According to our results, if the reported detections [17,18] of the bispectrum in the COBE map were the cosmological origin, then MAP and Planck would detect the primary bispectrum much more significantly. Although Banday, Zaroubi and Górski [19] pointed out the one of those detections [17] could be accounted for by the experimental systematic effects of COBE, the other [18] is claimed to be significant even after removing such the systematics.

Although we have not discussed so far, the spatial distribution of emissions from interstellar dust is a potential source of the microwave non-Gaussianity. Since it is very hard to estimate the bispectrum analytically, the dust map compiled by Schlegel, Finkbeiner and Davis [47] could be used to estimate the dust bispectrum. For example, we found that the dimensionless skewness parameter defined by $\langle (\Delta T)^3 \rangle / \langle (\Delta T)^2 \rangle^{3/2}$ is as large as 51. We used the publicly available HEALPix-formatted [48] 100 μm map which contains 12,582,912 pixels without sky cut. The mean intensity in the map was 14.8 MJy sr^{-1}. Of course, this skewness is largely an overestimate for the CMB measurement in reality; we need to cut a fraction of sky which contains the Galactic plane, and then this will greatly reduce the non-Gaussianity. Nevertheless, residual non-Gaussianity is still a source of the microwave bispectrum, and has to be taken into account. Moreover, the form of the bispectrum measured in the dust map would reflect the physics of interstellar dust, which is highly uncertain at present, and thus studying the interstellar dust bispectrum would be challenging field.

ACKNOWLEDGMENTS

[1] L. Verde, L. Wang, A. F. Heavens and M. Kamionkowski, Mon. Not. R. Astron. Soc. **313**, 141 (2000).

[2] K. Sato, Mon. Not. R. Astron. Soc. **195**, 467 (1981); Phys. Lett. **99B**, 66 (1981).

[3] A. Guth, Phys. Rev. D **23**, 347 (1981).

[4] A. Albrecht and P. J. Steinhardt, Phys. Rev. Lett. **48**, 1220 (1982).

[5] A. D. Linde, Phys. Lett. **108B**, 389 (1982).

[6] A. Guth and S. Y. Pi, Phys. Rev. Lett. **49**, 1110 (1982).

[7] S. Hawking, Phys. Lett. **115B**, 295 (1982).

[8] J. M. Bardeen, P. J. Steinhardt and M. S. Turner, Phys. Rev. D **28**, 679 (1983).

[9] A. A. Starobinsky, Phys. Lett. **117B**, 175 (1982).

[10] A. A. Starobinsky, in *Field Theory, Quantum Gravity, and Strings*, edited by H. T. de Vega and N. Sanchez, Lecture Notes in Physics, Vol. 246 (Springer-Verlag, Berlin, 1986), p.107.

[11] D. S. Salopek and J. R. Bond, Phys. Rev. D **42**, 3936 (1990); *ibid.* **43**, 1005 (1991).

[12] A. Gangui, F. Lucchin, S. Matarrese and S. Mollerach, Astrophys. J. **430**, 447 (1994).

[13] E. Calzetta and B. L. Hu, Phys. Rev. D **52**, 6770 (1995).

[14] A. Matacz, Phys. Rev. D **55**, 1860 (1997); *ibid.* **56**, R1836 (1997).

[15] L. Kofman, G. R. Blumenthal, H. Hodges and J. R. Primack, in *Large-Scale Structures and Peculiar Motions in the Universe*, edited by D. W. Latham and L. N. daCosta, ASP Conference Series, Vol. 15, 1991, p.339.

[16] A. Kogut, A. J. Banday, C. L. Bennett, K. M. Gorski, G. Hinshaw, G. F. Smoot and E. L. Wright, Astrophys. J. Lett. **464**, L29 (1996).

[17] P. G. Ferreira, J. Magueijo and K. M. Górski, Astrophys. J. Lett. **503**, L1 (1998).

[18] J. Magueijo, Astrophys. J. Lett. **528**, L57 (2000).

[19] A. J. Banday, S. Zaroubi and K. M. Górski, Astrophys. J. **533**, 575 (2000).

[20] D. N. Spergel and D. M. Goldberg, Phys. Rev. D **59**, 103001 (1999).

[21] D. M. Goldberg and D. N. Spergel, Phys. Rev. D **59**, 103002 (1999).

[22] A. Cooray and W. Hu, Astrophys. J. **534**, 533 (2000).

[23] W. Hu, Phys. Rev. D **62**, 043007 (2000).

[24] J. R. Bond, G. Efstathiou and M. Tegmark, Mon. Not. R. Astron. Soc. **291**, L33 (1997).

[25] L. Wang and M. Kamionkowski, Phys. Rev. D **61**, 063504 (2000).

[26] T. Pyne and S. M. Carroll, Phys. Rev. D **53**, 2920 (1996).

[27] U. Seljak and M. Zaldarriaga, Astrophys. J. **469**, 437 (1996).

[28] E. F. Bunn and M. White, Astrophys. J. **480**, 6 (1997).

[29] Ya. B. Zel'dovich and R. A. Sunyaev, Astrophys. Space. Sci. **4**, 301 (1969).

[30] F. M. Persi, D. N. Spergel, R. Cen and J. P. Ostriker, Astrophys. J. **442**, 1 (1995).

[31] R. Cen and J. Ostriker, Astrophys. J. **514**, 1 (1999).

[32] A. Refregier, E. Komatsu, D. N. Spergel and U. Pen, Phys. Rev. D **61**, 123001 (2000).

[33] V. Springel, M. White and L. Hernquist, preprint, astro-ph/0008133.

[34] P. Zhang and U. Pen, preprint, astro-ph/0007462.

[35] L. Toffolatti, F. Argüeso Gómez, G. De Zotti, P. Mazzei, A. Franceschini, L. Danese and C. Burigana, Mon. Not. R. Astron. Soc., **297**, 117 (1998).

[36] A. Refregier, D. N. Spergel and T. Herbig, Astrophys. J. **531**, 31 (2000).

[37] X. Luo, Astrophys. J. Lett. **427**, L71 (1994).

[38] A. F. Heavens, Mon. Not. R. Astron. Soc., **299**, 805 (1998).

[39] A. Gangui and J. Martin, Mon. Not. R. Astron. Soc., **313**, 323 (2000); Phys. Rev. D **62**, 103004 (2000).

[40] L. Knox, Phys. Rev. D **48**, 3502 (1995).

[41] C. L. Bennett, et al., Astrophys. J. Lett. **464**, L1 (1996).

[42] U. Seljak, Astrophys. J. **463**, 1 (1996).

[43] T. Kitayama and Y. Suto, Astrophys. J. **490**, 557 (1997).

[44] M. Srednicki, Astrophys. J. Lett. **416**, L1 (1993).

[45] M. Tegmark and G. Efstathiou, Mon. Not. R. Astron. Soc. **281**, 1297 (1996).

[46] A. Cooray, W. Hu and M. Tegmark, Astrophys. J. **540**, 1 (2000).

[47] D. J. Schlegel, D. P. Finkbeiner and M. Davis, Astrophys. J. **500**, 525 (1998).

[48] K. M. Górski, F. Hivon and B. D. Wandelt, in *Proceedings of the MPA/ESO Conference on Evolution of Large-Scale Structure: from Recombination to Garching*, edited by A. J. Banday, R. K. Sheth and L. N. daCosta, (1998).

TABLE I. The Fisher matrix F_{ij} (Eq.(51)). i and j denote components listed in the first row and the first column, respectively. $\overline{T}_{\rho 0}$ is in units of 1 keV, $b_{25}^{ps} \equiv b^{ps}/10^{-25}$, and $b_{27}^{ps} \equiv b^{ps}/10^{-27}$.

COBE	primary	SZ–lensing	point sources
primary	$4.2 \times 10^{-6} \ f_{NL}^2$	$-4.0 \times 10^{-7} \ f_{NL} j_\nu \overline{T}_{\rho 0} b_{gas}$	$-1.0 \times 10^{-9} \ f_{NL} b_{25}^{ps}$
SZ–lensing		$1.3 \times 10^{-7} \ (j_\nu \overline{T}_{\rho 0} b_{gas})^2$	$3.1 \times 10^{-10} \ j_\nu \overline{T}_{\rho 0} b_{gas} b_{25}^{ps}$
point sources			$1.1 \times 10^{-12} \ (b_{25}^{ps})^2$
MAP			
primary	$3.4 \times 10^{-3} \ f_{NL}^2$	$2.6 \times 10^{-3} \ f_{NL} j_\nu \overline{T}_{\rho 0} b_{gas}$	$2.4 \times 10^{-3} \ f_{NL} b_{25}^{ps}$
SZ–lensing		$0.14 \ (j_\nu \overline{T}_{\rho 0} b_{gas})^2$	$0.31 \ j_\nu \overline{T}_{\rho 0} b_{gas} b_{25}^{ps}$
point sources			$5.6 \ (b_{25}^{ps})^2$
Planck			
primary	$3.8 \times 10^{-2} \ f_{NL}^2$	$7.2 \times 10^{-2} \ f_{NL} j_\nu \overline{T}_{\rho 0} b_{gas}$	$1.6 \times 10^{-2} \ f_{NL} b_{27}^{ps}$
SZ–lensing		$39 \ (j_\nu \overline{T}_{\rho 0} b_{gas})^2$	$5.7 \ j_\nu \overline{T}_{\rho 0} b_{gas} b_{27}^{ps}$
point sources			$2.7 \times 10^3 \ (b_{27}^{ps})^2$

TABLE II. The inverse Fisher matrix F_{ij}^{-1}. i and j denote components listed in the first row and the first column, respectively. $\overline{T}_{\rho 0}$ is in units of 1 keV, $b_{25}^{ps} \equiv b^{ps}/10^{-25}$, and $b_{27}^{ps} \equiv b^{ps}/10^{-27}$.

COBE	primary	SZ–lensing	point sources
primary	$3.5 \times 10^5 \ f_{NL}^{-2}$	$1.1 \times 10^6 \ (f_{NL} j_\nu \overline{T}_{\rho 0} b_{gas})^{-1}$	$1.3 \times 10^7 \ (f_{NL} b_{25}^{ps})^{-1}$
SZ–lensing		$3.1 \times 10^7 \ (j_\nu \overline{T}_{\rho 0} b_{gas})^{-2}$	$-7.8 \times 10^9 \ (j_\nu \overline{T}_{\rho 0} b_{gas} b_{25}^{ps})^{-1}$
point sources			$3.1 \times 10^{12} \ (b_{25}^{ps})^{-2}$
MAP			
primary	$3.0 \times 10^2 \ f_{NL}^{-2}$	$-6.1 \ (f_{NL} j_\nu \overline{T}_{\rho 0} b_{gas})^{-1}$	$0.21 \ (f_{NL} b_{25}^{ps})^{-1}$
SZ–lensing		$8.4 \ (j_\nu \overline{T}_{\rho 0} b_{gas})^{-2}$	$-0.46 \ (j_\nu \overline{T}_{\rho 0} b_{gas} b_{25}^{ps})^{-1}$
point sources			$0.21 \ (b_{25}^{ps})^{-2}$
Planck			
primary	$26 \ f_{NL}^{-2}$	$-4.9 \times 10^{-2} \ (f_{NL} j_\nu \overline{T}_{\rho 0} b_{gas})^{-1}$	$-5.7 \times 10^{-5} \ (f_{NL} b_{27}^{ps})^{-1}$
SZ–lensing		$2.6 \times 10^{-2} \ (j_\nu \overline{T}_{\rho 0} b_{gas})^{-2}$	$-5.4 \times 10^{-5} \ (j_\nu \overline{T}_{\rho 0} b_{gas} b_{27}^{ps})^{-1}$
point sources			$3.7 \times 10^{-4} \ (b_{27}^{ps})^{-2}$

TABLE III. The signal-to-noise ratio $(S/N)_i$ (Eq.(52)). i denotes a component listed in the first row. $\overline{T}_{\rho 0}$ is in units of 1 keV, $b_{25}^{ps} \equiv b^{ps}/10^{-25}$, and $b_{27}^{ps} \equiv b^{ps}/10^{-27}$.

	primary	SZ–lensing	point sources
COBE	$1.7 \times 10^{-3} \ f_{NL}$	$1.8 \times 10^{-4} \ |j_\nu| \overline{T}_{\rho 0} b_{gas}$	$5.7 \times 10^{-7} \ b_{25}^{ps}$
MAP	$5.8 \times 10^{-2} \ f_{NL}$	$0.34 \ |j_\nu| \overline{T}_{\rho 0} b_{gas}$	$2.2 \ b_{25}^{ps}$
Planck	$0.19 \ f_{NL}$	$6.2 \ |j_\nu| \overline{T}_{\rho 0} b_{gas}$	$52 \ b_{27}^{ps}$

TABLE IV. The degradation parameter d_i (Eq.(54)) and correlation r_{ij} (Eq.(53)) matrix. i and j denote components listed in the first row and the first column, respectively. d_i for $i = j$, while r_{ij} for $i \neq j$.

COBE	primary	SZ–lensing	point sources
primary	1.46	$0.33\ \mathrm{sgn}(j_\nu)$	1.6×10^{-2}
SZ–lensing		3.89	$-0.79\ \mathrm{sgn}(j_\nu)$
point sources			3.45
MAP			
primary	1.01	$-0.12\ \mathrm{sgn}(j_\nu)$	2.7×10^{-2}
SZ–lensing		1.16	$-0.35\ \mathrm{sgn}(j_\nu)$
point sources			1.14
Planck			
primary	1.00	$-5.9 \times 10^{-2}\ \mathrm{sgn}(j_\nu)$	-5.8×10^{-4}
SZ–lensing		1.00	$-1.8 \times 10^{-2}\ \mathrm{sgn}(j_\nu)$
point sources			1.00

TABLE V. The minimum non-linear coupling constant f_{NL} required to detect the primary non-Gaussianity by the bispectrum and the skewness with the signal-to-noise ratio of > 1. These estimates include the effects of cosmic variance, detector noise, and foreground sources.

Experiments	f_{NL} (Bispectrum)	f_{NL} (Skewness)
COBE	600	800
MAP	20	80
Planck	5	70
Ideal	3	60